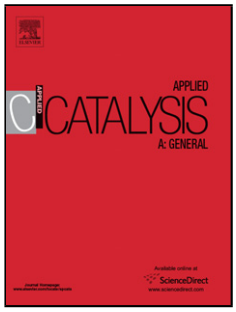


Title: Selective Gas Phase Hydrogenation of *p*-Nitrobenzonitrile to *p*-Aminobenzonitrile over Zirconia Supported Gold

Author: Xiaodong Wang Yufen Hao Mark A. Keane

PII: S0926-860X(15)30258-1
DOI: http://dx.doi.org/doi:10.1016/j.apcata.2015.11.030
Reference: APCATA 15657

To appear in: *Applied Catalysis A: General*

Received date: 11-9-2015
Revised date: 13-11-2015
Accepted date: 15-11-2015

Please cite this article as: Xiaodong Wang, Yufen Hao, Mark A.Keane, Selective Gas Phase Hydrogenation of p-Nitrobenzonitrile to p-Aminobenzonitrile over Zirconia Supported Gold, Applied Catalysis A, General http://dx.doi.org/10.1016/j.apcata.2015.11.030

# Selective Gas Phase Hydrogenation of *p*-Nitrobenzonitrile to *p*-Aminobenzonitrile over Zirconia Supported Gold

**Xiaodong Wang[1], Yufen Hao and Mark A. Keane***

Chemical Engineering, School of Engineering & Physical Sciences,

Heriot-Watt University, Edinburgh EH14 4AS, Scotland

*corresponding author

Tel: +44(0)131 451 4719, e-mail: M.A.Keane@hw.ac.uk

[1]present address: School of Engineering, University of Aberdeen, Aberdeen AB24 3UE, Scotland

**Graphical abstract**

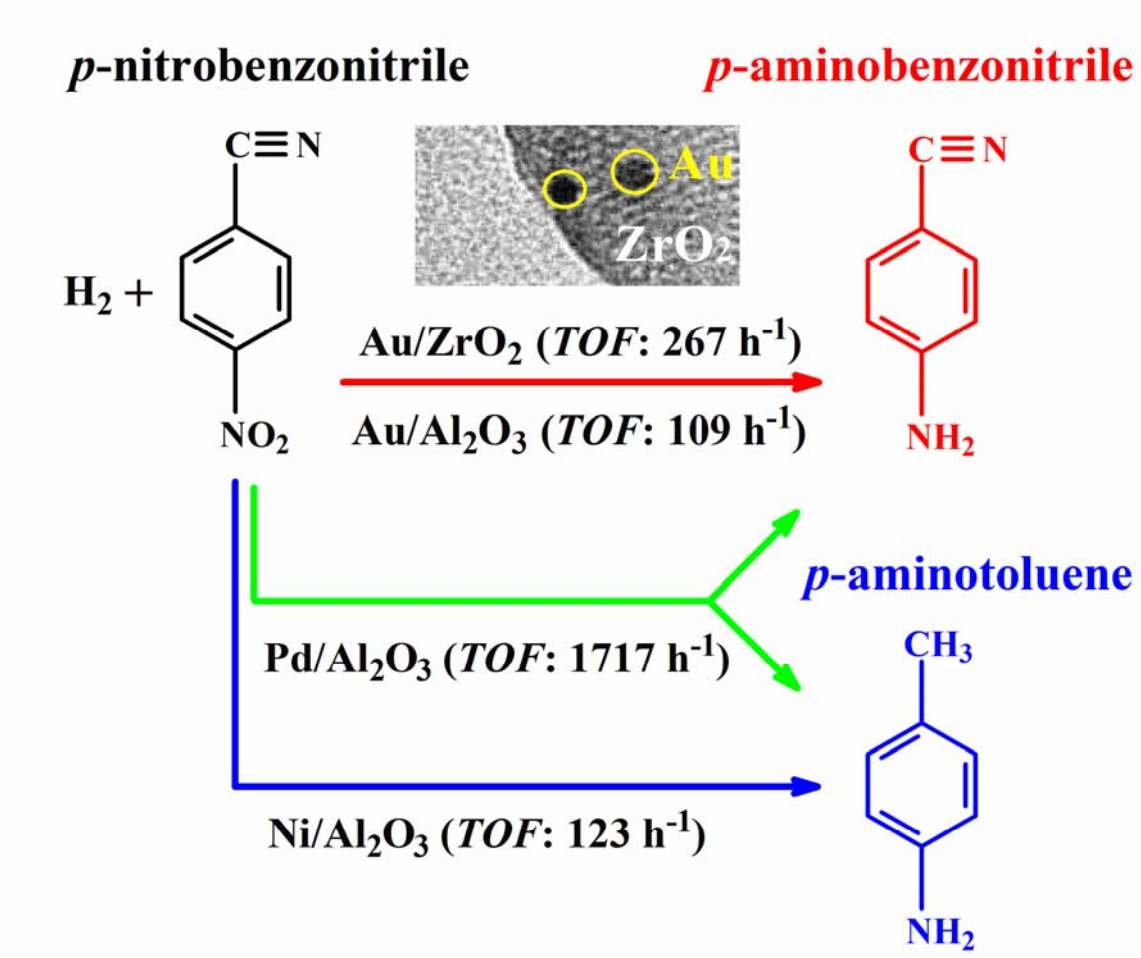

Highlights

- First report of *p*-nitrobenzonitrile gas phase hydrogenation over supported Au
- 100% yield of *p*-aminobenzonitrile over $Au/ZrO_2$ and $Au/Al_2O_3$
- $Au/ZrO_2$ outperforms $Au/Al_2O_3$, $Pd/Al_2O_3$ and $Ni/Al_2O_3$
- Tetragonal → monoclinic $ZrO_2$ on introduction of Au by deposition-precipitation

**Abstract**

The catalytic action of $Au/ZrO_2$ in the gas phase hydrogenation of *p*-nitrobenzonitrile (*p*-NBN) to *p*-aminobenzonitrile (*p*-ABN) has been assessed against $Au/Al_2O_3$. Crystalline $ZrO_2$ was prepared by precipitation of $ZrOCl_2$ with aqueous $NH_3$ and calcined to generate tetragonal and monoclinic phases. Catalyst and support were characterised by surface area/porosity, temperature-programmed reduction (TPR), $H_2$ chemisorption/temperature programmed desorption (TPD), X-ray diffraction (XRD), transmission electron microscopy (TEM) and X-ray photoelectron spectroscopy (XPS) measurements. Higher calcination temperatures (673-973 K) increased the monoclinic $ZrO_2$ content with a decrease in surface area and pore volume. Introduction of Au by deposition-precipitation resulted in tetragonal→monoclinic transformation with post-TPR formation of Au particles in the 3-13 nm size range and electron transfer from $ZrO_2$. Reaction over $Au/ZrO_2$ delivered 100% *p*-ABN yield with higher turnover frequency (267 $h^{-1}$) than $Au/Al_2O_3$ (109 $h^{-1}$) attributed to greater $H_2$ chemisorption capacity under reaction conditions and enhanced $-NO_2$ activation. $Au/ZrO_2$ outperformed benchmark $Pd/Al_2O_3$ and $Ni/Al_2O_3$, which generated *p*-aminotoluene *via* subsequent hydrogenation/hydrogenolysis.

*Keywords*: selective hydrogenation; $Au/ZrO_2$; $Au/Al_2O_3$; *p*-nitrobenzonitrile; *p*-aminobenzonitrile.

## 1. Introduction

Zirconia ($ZrO_2$) has found widespread application in catalysis, structural engineering and biomedicine [1,2]. This study focuses on $ZrO_2$ as a metal (Au) catalyst support [3]. We should note the use of $ZrO_2$ to promote transesterification [4], acylation [5], bromination [6], carbomagnetisation [7] and the reaction of hydrazines with alkynes [8]. Nevertheless, $ZrO_2$ has principally been employed as a support due to its adjustable (*via* variations in synthesis, precursor and use of dopants) structural and chemical properties [9]. Notable examples include $ZrO_2$ supported Fe [10] and Co [11] in Fischer-Tropsch synthesis, steam reforming over Pt [12] and Ni [13] and use of supported Cu to treat vehicular exhaust gas [14]. The development of supported Au in chemoselective catalysis is now the subject of appreciable research as highlighted in a series of reviews [15-18]. Gold on zirconia is a relatively unexplored catalyst formulation but has been applied in low temperature water gas shift reaction [19], CO oxidation [20] and the hydrogenation of $CO_2$ [21], 1,3-butadiene, acrolein and crotonaldehyde [22]. Koeppel *et al*. [23] demonstrated that crystalline (relative to amorphous) $ZrO_2$ delivered enhanced performance in $CO_2$ hydrogenation. Zirconia exhibiting comparable size to the supported metal phase has shown a superior response in CO oxidation ($Au/ZrO_2$ [20]) and steam reforming ($Ni/ZrO_2$ [24]). Of relevance to this study, He *et al*. have achieved high selectivities to the chlorinated amine in the liquid phase hydrogenation of *p*- and *o*-chloronitrobenzene and 2,5-dichloronitrobenzene over $Au/ZrO_2$ [25].

Drawing on these findings, we have prepared a crystalline $ZrO_2$ supported Au catalyst for use in the gas phase hydrogenation of *p*-nitrobenzonitrile (*p*-NBN). The target amine product

(*p*-aminobenzonitrile (*p*-ABN)) is used in the commercial production of a diversity of agrochemicals, pharmaceuticals, dyestuffs, urethanes and fine chemicals [26]. The literature [27-33] dealing with *p*-NBN hydrogenation is limited and has focused on batch liquid phase reactions at elevated pressures (up to 6 MPa [31]) where high selectivity to *p*-ABN is challenging. We can flag selectivities up to 97% achieved using $Au/TiO_2$ and $Au/Fe_2O_3$ at near complete *p*-NBN conversion [27]. We provide here the first reported gas phase continuous hydrogenation of *p*-NBN over supported Au. We have also examined the catalytic action of $Au/Al_2O_3$ for comparison purposes as this catalyst system has been applied in (aromatic [34] and aliphatic [35]) nitro, carbonyl [36] and C=C/C≡C [37] hydrogenation. Supported Ni [31] and Pd [38] serve as benchmark catalysts in this work. Purity of the target amine is an important consideration given the difficult separation (by distillation) of hydrogenation products with similar boiling points [31]. Consequently, we have set out as an explicit goal of this study to achieve exclusive selectivity to *p*-ABN.

## 2. Experimental

### *2.1 Chemicals*

Zirconium (IV) oxychloride octahydrate ($ZrOCl_2 \cdot 8H_2O$, ≥ 99.5%) and Au (III) chloride hydrate (99.999%) were obtained from Sigma-Aldrich and the ammonia solution (35% w/w $NH_3$) from Fisher Scientific. All gases were of high purity (99.9%, BOC gases). The reactants (*p*-nitrobenzonitrile (≥ 97%), nitrobenzene (≥ 99%) and benzonitrile (≥ 99%), Sigma-Aldrich), solvent (1-butanol, Riedel-de Haen (≥ 99.5%)), urea (Riedel-de Häen (≥ 99%)) and $\gamma$-$Al_2O_3$ support (Puralox, Condea Vista Co.) were used as received.

*2.2 Catalyst preparation*

The zirconia support precursor was prepared by precipitation with dropwise addition of $ZrOCl_2 \cdot 8H_2O$ (0.1 M) to aqueous $NH_3$ (2.5 M) under vigorous stirring. Temporal pH changes were measured with a crystal-body electrode coupled to a data logging and collection system (Pico Technology). The resultant hydrogel was washed thoroughly with deionised water until free of chloride ions ($AgNO_3$ test), dried at 373 K for 24 h and calcined (1 K $min^{-1}$) in 60 $cm^3$ $min^{-1}$ air at 673-973 K for 5 h. Gold (nominal 1% w/w) loaded $ZrO_2$ (calcined at 673 K) was prepared by deposition-precipitation. Urea as basification agent was added (100-fold excess) to a solution of $HAuCl_4$ ($5.1 \times 10^{-3}$ M), $ZrO_2$ introduced and the suspension stirred (300 rpm) and heated to 353 K (2 K $min^{-1}$) for 4 h. The solid was separated by centrifugation, washed with deionised water and dried in He (60 $cm^3$ $min^{-1}$) at 373 K (2 K $min^{-1}$) for 5 h. For comparison purposes, $Au/Al_2O_3$ (1 w/w %) was prepared by standard impregnation using aqueous $HAuCl_4$ ($7.3 \times 10^{-3}$ M) where the slurry was heated at 2 K $min^{-1}$ to 353 K and agitated (600 rpm) in a He purge. Benchmark $Pd/Al_2O_3$ and $Ni/Al_2O_3$ were synthesised by impregnation as described elsewhere [39]. Samples were sieved to 75 μm average particle diameter and metal loading determined by inductively coupled plasma-optical emission spectrometry (Vista-PRO, Varian Inc.).

*2.3 Catalyst characterisation*

The pH associated with the point of zero charge ($pH_{PZC}$) of $ZrO_2$ was determined using the potentiometric mass titration technique [40]. Three different masses of $ZrO_2$ (0.025, 0.050 and 0.075 g) were immersed in 50 $cm^3$ 0.1 M NaCl to which a known amount of NaOH (0.1 M)

was added to adjust the pH to 11. Titration was performed under continuous agitation in He with HCl (0.1 M) as titrant; temporal changes to pH were measured as described above. Nitrogen adsorption-desorption isotherms were obtained at 77 K using the commercial Micromeritics Gemini 2390 automated system. Specific surface area was obtained from the standard BET method and average pore size, cumulative pore volume and pore size distribution obtained from BJH analysis; samples were outgassed at 423 K for 1 h prior to measurements. Temperature programmed reduction (TPR) and $H_2$ chemisorption were recorded on the commercial CHEMBET 3000 (Quantachrome Instrument) unit; data acquisition/manipulation employed the TPR Win$^{TM}$ software. The sample was loaded into a U-shaped quartz cell (100 mm × 3.76 mm i.d.) and heated in 17 cm$^3$ min$^{-1}$ (Brooks mass flow controlled) 5% v/v $H_2/N_2$ at 2 K min$^{-1}$ to 473 or 10 K min$^{-1}$ to 1073 K. Following TPR (to 473 K), samples were swept with 65 cm$^3$ min$^{-1}$ $N_2$ for 1.5 h, cooled to ambient or reaction (423 K) temperature and subjected to $H_2$ chemisorption using a pulse (10 μl) titration procedure. Hydrogen pulse introduction was repeated until the signal area was constant, indicating surface saturation. Powder X-ray diffractograms (XRD) were recorded on a Bruker/Siemens D500 incident X-ray diffractometer using Cu Kα radiation. The sample was scanned at a rate of 0.02º step$^{-1}$ over 5º ≤ 2$\theta$ ≤ 85º. Diffractograms were identified against JCPDS-ICDD reference standards, *i.e.* Au (04-0784), $ZrO_2$ (tetragonal (50-1089) and monoclinic (37-1487)). The monoclinic fraction was calculated from the integrated intensities ($I$) of the (111) and (-111) monoclinic ($m$-$ZrO_2$ ) and (011) tetragonal ($t$-$ZrO_2$) signals [41],

$$X_m = \frac{I_m(-111)+I_m(111)}{I_m(-111)+I_m(111)+I_t(011)}; \qquad V_m = \frac{1.31 \times X_m}{1+0.31 \times X_m} \tag{1}$$

where $X_m$ represents the intensity ratio and $V_m$ the fraction of monoclinic $ZrO_2$. Transmission electron microscopy was conducted on a JEOL JEM 2011 HRTEM unit with a UTW energy dispersive X-ray (EDX) detector (Oxford Instruments) operated at an accelerating voltage of 200 kV and Gatan Digital Micrograph 3.4 for data acquisition/manipulation. Samples were dispersed in acetone and deposited on a holey carbon/Cu grid (300 Mesh). Metal particle size is given as a surface area-weighted mean ($d_{TEM}$) according to

$$d_{TEM} = \frac{\sum_i n_i d_i^3}{\sum_i n_i d_i^2} \quad (2)$$

where $n_i$ is the number of particles of diameter $d_i$. XPS spectra were collected on a SPECS (Phoibos MCD 150) X-ray photoelectron spectrometer using an Al K$\alpha$ ($hv$ = 1486.6 eV) x-ray source. Binding energies were calibrated with respect to the C-C/C-H components of the C 1*s* peak (binding energy = 284.7 eV); spectra processing employed Casa XPS software.

*2.4 Catalytic procedure*

Reactions were carried out *in situ,* following activation (at 2 K $min^{-1}$ to 473 K in 60 $cm^3$ $min^{-1}$ $H_2$ for 1 h) in a continuous flow fixed bed vertical glass reactor (i.d. = 15 mm, $l$ = 600 mm) at 423 K and 1 atm. The catalytic reactor and operating conditions to ensure negligible heat/mass transport limitations have been fully described elsewhere [42] but features pertinent to this study are given below. A layer of borosilicate glass beads served as preheating zone, ensuring that the organic reactants were vaporised and reached reaction temperature before contacting the catalyst. Isothermal conditions (±1 K) were ensured by diluting the catalyst bed with ground glass (75 μm). Reaction temperature was continuously monitored by a

thermocouple inserted in a thermowell within the catalyst bed. The *p*-NBN reactant was delivered as a butanolic solution *via* a glass/teflon air-tight syringe and teflon line using a microprocessor controlled infusion pump (Model 100 kd Scientific) at a fixed calibrated flow rate. A co-current flow of *p*-NBN and $H_2$ was maintained at $GHSV = 2 \times 10^4$ $h^{-1}$ with an inlet *p*-NBN molar flow ($F$) in the range $4.0\times10^{-5}$–$7.2\times10^{-5}$ mol $h^{-1}$; molar Au ($n_{Au}$) to $F$ content spanned the range $1.6\times10^{-3}$–$14\times10^{-2}$ h. In blank tests, passage of *p*-NBN in a stream of $H_2$ through the empty reactor or over the supports did not result in any detectable conversion. The reactor effluent was frozen in a liquid nitrogen trap for analysis using a Perkin-Elmer Auto System XL gas chromatograph equipped with a programmed split/splitless injector and FID, employing a DB-1 50 m × 0.20 mm i.d. 0.33 μm film thickness capillary column (J&W Scientific). Repeated reactions with different samples from the same batch of catalyst delivered raw data that were reproducible to ± 7%.

## 3. Results and Discussion

### *3.1 Catalyst characteristics*

#### *3.1.1 $ZrO_2$ synthesis and characterisation*

Solution pH during $ZrO_2$ synthesis exhibited a temporal decrease from 11.8 to 9.3 (Fig. 1(A)) at which point precipitation was complete [43]. Synthesis was conducted under basic conditions to generate a hydrous precursor that can be converted to $ZrO_2$ with higher surface area than achieved at low pH [43]. The as prepared $ZrO_2$ (after drying) exhibited a surface area (280 $m^2$ $g^{-1}$, Table 1) close to that reported for similar preparation conditions [44,45]. The XRD pattern (not shown) did not exhibit any diffraction peaks. It has been observed elsewhere that calcination is required at temperatures in excess of 573 K to generate a crystalline phase [48].

Increasing calcination temperature served to lower surface area and total pore volume (Table 1). Mercera *et al.* [45] noted that the specific surface area fell drastically (by 97%) after calcination to 1123 K and attributed this to crystallite growth with an accompanying phase transformation and/or thermally induced sintering. The XRD patterns for calcined $ZrO_2$ (Fig. 1(B)) exhibit the three main characteristic peaks [47] for monoclinic ((-111), (111)) and tetragonal (011) phases based on the JCPDS references (37-1484 and 50-1089). The intensity of the tetragonal (011) peak relative to monoclinic (-111) and (111) signals was lower at higher temperatures, indicating a thermal dependence of phase composition. The monoclinic content obtained by applying eq. (1) is given in Table 1. A near pure monoclinic phase was obtained at 973 K as reported by Xu and co-workers [49]. Chuah *et al.* [43] have shown that $ZrO_2$ phase composition is sensitive to precipitation temperature, pH and thermal treatment. A mixed phase that was predominantly monoclinic (50-78%) was formed at synthesis temperatures of 303-353 K in basic media with subsequent calcination at 773 K. We observed (Table 1) an increase in crystallite size at higher temperatures, which agrees with the findings of Stichert and Schuth [50].

Use of a high surface area support on which to anchor Au particles can ensure a well dispersed metal phase at the *nano*-scale required to deliver significant hydrogenation activity [51]. As $ZrO_2$ crystallinity is an important property, the sample resulting from calcination at 673 K (BET area = 104 $m^2\ g^{-1}$) was chosen as Au carrier. Nitrogen adsorption isotherms are given in Fig. 2(A) where the observed hysteresis is typical of (type IV) mesoporous materials. Pore size distribution (10–29 Å) and mean radius (19 Å) are diagnostic of a well-developed

mesopore framework [45]. In catalyst preparation by deposition-precipitation, the pH associated with the point of zero charge ($pH_{PZC}$) is a critical property that determines precursor-support interaction as a function of solution pH [40]. A $pH_{PZC}$ of 7.4 was determined experimentally for $ZrO_2$, which is within the range of values (6.2-8.5) reported elsewhere [52,53]. The $pH_{PZC}$ is dependent on $ZrO_2$ preparation and composition where a higher value (8.5) is associated with a monoclinic relative to tetragonal phase (6.2) [52].

*3.1.2 $Au/ZrO_2$ and $Au/Al_2O_3$ synthesis and characterisation*

The temporal pH variation in $Au/ZrO_2$ preparation is shown in Fig. 1(C) where the $pH_{PZC}$ of $ZrO_2$ (7.4) is identified by the dashed line. The initial pH drop is due to temperature induced $HAuCl_4$ hydrolysis [54]. Further increase in temperature (to 353 K) led to progressive decomposition of urea accompanied by an increase in pH to 6.5 after 4 h. As the solution pH remained below the $pH_{PZC}$, the support retained a net positive charge favouring interaction with anionic gold species ($AuCl_4^-$ and/or $Au(OH)Cl_3^-$) in solution [55] and the surface sites served as nucleation centres for Au deposition [56]. The incorporation of Au on $ZrO_2$ resulted in a decrease in surface area and pore volume (Table 1). Nitrogen isotherms and pore size distribution (Fig. 2(B)) largely converged with those recorded for $ZrO_2$ with an equivalent mean pore diameter (19 Å, Table 2). Alumina supported Au, carried through in this study for comparative purposes was characterised by a surface area (161 $m^2\ g^{-1}$, Table 2), total pore volume (0.36 $cm^3\ g^{-1}$) and average pore size (30 Å) in line with a related $Au/Al_2O_3$ system [34].

Temperature programmed reduction (TPR) screening (to 1073 K, Fig. 3(A)) was conducted to assess reducibility of $ZrO_2$ and $Au/ZrO_2$. There was no detectable $H_2$ consumption

during TPR of $ZrO_2$, which agrees with an earlier report [57]. The TPR profile of $Au/ZrO_2$ exhibited two peaks where the $H_2$ consumed (Table 2) associated with the lower temperature signal matched the requirement for $Au^{3+} \rightarrow Au^0$ reduction. The peak at 865 K can be attributed to a partial reduction of (surface) $Zr^{4+}$ (to $Zr^{3+}$). Xu *et al*. have also recorded two reduction peaks (at 483–503 and 823–853 K) for $Au/ZrO_2$ precalcined at 573 K [58]. Our results suggest that the incorporation of Au facilitates support reduction as has been proposed for $Au/CeO_2$ [35], $Au/Ce_xZr_{1-x}O_2$ [59] and $Au/TiO_2$ [60]. Grau-Crespo and co-workers [61], applying density functional theory, have demonstrated that the presence of Au in the $ZrO_2$ lattice impacts on surface redox properties under reducing conditions. A final reduction temperature of 473 K was accordingly employed to reduce the supported Au precursor without modifying the $ZrO_2$ support. The associated TPR profile (Fig. 3(B)) exhibits a single peak (452 K) at a higher temperature maximum ($T_{max}$) than the reduction of $Au/Al_2O_3$ (417 K) suggesting stronger metal/support interaction in $Au/ZrO_2$ [60]. Lopez-Sanchez and Lennon have related the catalytic performance of $Au/TiO_2$ and $Au/Fe_2O_3$ in propyne hydrogenation to the strength of Au interaction with the carrier [62]. Liu and Yang proposed that weaker Au support-interactions (lower TPR $T_{max}$) led to inferior activity [63].

The XRD pattern of activated $Au/ZrO_2$ (Fig. 1(D)) coincides with the starting $ZrO_2$ support (Profile I, Fig. 1(B)) in terms of peak position. However, the intensity of the tetragonal (011) signal ($2\theta$ = 30.3°) was markedly reduced with a consequent increase in monoclinic content (from 58 to 88%) due to the incorporation of Au. Such a phase change in the support alone would require elevated calcination temperature, accompanied by a significantly lower

BET surface area (see Table 1). As the XRD pattern for $Au/ZrO_2$ as prepared matched that obtained for the activated catalyst the support phase change was not the result of the TPR step. Xie and co-workers [47] have reported that exposure of tetragonal $ZrO_2$ to 3 kPa $H_2O$ or immersion in water at 298 K resulted in a transformation to the monoclinic form without loss of surface area, an effect that they attributed to differences in surface free energy between the two phases after water adsorption. In our $Au/ZrO_2$ preparation, the support was contacted with an aqueous Au salt solution with pH and temperature variations for up to 4 h that must contribute to the phase change. Representative TEM images and the Au particle size distributions for $Au/ZrO_2$ (A) and $Au/Al_2O_3$ (B) are provided in Fig. 4. The micrographs reveal discrete Au particles at the nano-scale that exhibit a quasi-spherical shape with comparable surface area weighted mean diameters (7-8 nm, Table 2).

The dynamics of $H_2$-Au interactions has yet to be well established but the consensus that emerges suggests a high activation energy barrier for dissociative adsorption [64]. Dissociative chemisorption has been associated with low coordination Au sites and shows a dependence on Au size [51,65]. Ambient temperature $H_2$ chemisorption on $Au/ZrO_2$ was measurably greater (by a factor of 3) than that recorded for $Au/Al_2O_3$ (Table 2). Hydrogen adsorption is an activated process and enhanced at higher temperature (to 423 K, Table 2). Bus *et al*. also recorded an increase in $H_2$ chemisorption with increasing temperature (from 298 to 373 K) [66]. Given the equivalence of Au size, the differences in $H_2$ uptake may be linked to electronic structure. Boronat *et al*. [67] have proposed from density functional calculations that Au atoms (on $TiO_2$) active for $H_2$ dissociation must be neutral or with a net charge close to zero and located at corner

or edge positions. In earlier work, we have established that Au electronic structure [34,60] is an important property that determines hydrogenation performance. XPS profiles over the Au 4*f* binding energy (BE) region are presented in Fig. 5. Analysis of $Au/ZrO_2$ generated peaks at 83.5 eV and 87.3 eV that compare with Au $4f_{7/2}$ (83.6 eV) and $4f_{5/2}$ (87.6 eV) BE values given elsewhere [68]. The $Au/Al_2O_3$ profile exhibited signals at 83.2 eV and 87.0 eV that also match the literature [69]. Both catalysts exhibited a shift to lower BE relative to the reference metallic Au $4f_{7/2}$ (84.0 eV), indicating electron transfer from the support to nano-scale Au [70]. An electron-rich ($Au^{\delta-}$) phase is accordingly generated on both supports with a greater degree of electron transfer (on the basis of BE values) from $Al_2O_3$. It has been demonstrated by Ealet and Gillet that electronegative Au acts as an electron acceptor with respect to Al, inducing electron transfer [71]. A lower charge density associated with Au on $ZrO_2$ relative to $Al_2O_3$ may account for enhanced $H_2$ chemisorption on $Au/ZrO_2$. Shimizu *et al*. [72] have proposed that $H_2$ dissociation at the Au-support interface generates $H^{\delta-}$ on Au and $H^{\delta+}$ stabilised by the support oxygen. The greater electron density at Au sites on $Al_2O_3$ may inhibit this process due to repulsive effects leading to lower overall uptake. Hydrogen release during TPD from both catalysts is similar and far exceeded the chemisorption measurements (Table 2), suggesting the occurrence of spillover hydrogen during TPR. Spillover is well established for supported metals [73], including Au [34,35,59], where $H_2$ dissociates at metal sites, generating H atoms that diffuse or "spillover" onto the support.

*3.2 Catalytic response*

The hydrogenation of *p*-NBN presents enormous selectivity challenges, generating up to

15 intermediates and products as established by Koprivova and Cerveny [31]. While an overall reaction scheme can involve disproportionation, reduction, condensation, hydrodenitrogenation and hydrodecarbonation, a simplified pathway is presented in Fig. 6 that applies to the published (liquid phase) catalytic studies [31,32]. Conversion of *p*-NBN to the target *p*-ABN generates partially hydrogenated *p*-nitrosobenzonitrile and *p*-(cyanophenyl)-hydroxylamine [28] as intermediates that undergo condensation to give 4,4′-dicyanoazobenzene [31]. The *p*-ABN formed can be hydrated to *p*-aminobenzamide and/or further hydrogenated to *p*-aminobenzylimine and *p*-aminobenzylamine [31] with subsequent hydrogenolysis to give *p*-aminotoluene (*p*-ATL) [31,32]. Condensation of *p*-aminobenzylimine and *p*-aminobenzylamine results in secondary amine (4,4'-diaminodibenzylamine) formation that can be converted to *p*-ATL. Fractional *p*-NBN conversion ($x_{p\text{-NBN}}$) is presented as a function of time on-stream in Fig. 7(A). The temporal activity response can be expressed in terms of the empirical relationship [34,40]

$$\frac{(x_{p-NBN} - x_0)}{(x_{3h} - x_0)} = \frac{\Delta t}{(\beta + \Delta t)} \tag{3}$$

where $x_{3h}$ represents conversion after 3 h on-stream and $\beta$ is a time scale fitting parameter. Fit convergence yields $x_0$ (initial conversion) used to derive the rate constant ($k$) according to

$$\ln(1 - x_0)^{-1} = k\left(\frac{n}{F}\right) \tag{4}$$

where $n/F$ has the physical significance of contact time. Linear relationships between $\ln(1\text{-}x_0)^{-1}$ and $n/F$ are shown in Fig. 7(B). The experimentally determined rate constants were normalised with respect to Au dispersion to give *p*-NBN turnover frequencies (*TOF*, $h^{-1}$). The catalytic

results can be compared in Table 3 where Au/$ZrO_2$ delivered a higher *TOF* relative to Au/$Al_2O_3$, which correlates with the greater $H_2$ chemisorption capacity under reaction conditions (Table 2). Moreover, the greater electron density associated with Au on $Al_2O_3$ can result in strong repulsive effects with respect to electron rich –$NO_2$ (as an electron withdrawing group) that inhibits nitro-group activation, lowering activity [34].

Both Au catalysts promoted exclusive production of *p*-ABN at every level of conversion ($x_{p\text{-}NBN}$ from 0 to 1, see Fig. 7(B)), *i.e.* 100% yield of the target amine. This is a significant finding as reaction exclusivity to *p*-ABN has not been reported previously. The only gas phase study with which we can compare our results dates from the 1950s where Hata and Watanabe [32] investigated the hydrogenation of various aromatic nitriles (including the three NBN isomers) over a Ni–Cu catalyst at 523-573 K and reported the formation of aniline, toluidine and ABN (< 32% yield). We did not observe any activity in the reaction of benzonitrile over Au/$ZrO_2$ or Au/$Al_2O_3$. In contrast, use of nitrobenzene as feed generated aniline where Au/$ZrO_2$ delivered a higher *TOF* (238 $h^{-1}$) than Au/$Al_2O_3$ (67 $h^{-1}$). This is consistent with the observed selectivity to *p*-NBN where the nitrile function remains unreacted and Au/$ZrO_2$ is intrinsically more active. Corma *et al*. employed Au catalysts [27] to convert NBN to ABN in the liquid phase and noted that Au/$TiO_2$ exhibited the highest selectivity (97%) for reaction at 25 atm and 413 K. That study did not include *TOF* values which we can relate to our measurements. The move from batch liquid to gas phase continuous operation is however significant in terms of increased throughput and energy efficiency where 100% yield at ambient pressure is an important sustainability consideration [74].

In order to further probe reaction selectivity, we employed $Pd/Al_2O_3$ and $Ni/Al_2O_3$ as benchmark catalysts (characterisation details provided elsewhere [39]) that have shown high activity in nitro-group [39] reduction; results are included in Table 3. Drawing on published work, application of Pd(II) acetate in liquid phase hydrogenation of *p*-NBN gave a 77% *p*-ABN yield [28] whereas Raney Ni was non-selective, generating (from *o*-NBN) a range of intermediates and by-products including *o*-aminobenzylamine, *o*-aminobenzamide, *o*-ATL, 3,3′-dicyanoazobenzene and 3,3′′-diaminodibenzylamine [31]. Gas phase reaction over $Pd/Al_2O_3$ delivered a significantly higher *TOF* relative to supported Au with full selectivity to *p*-ABN at low fractional *p*-NBN conversion ($x_{p\text{-NBN}} = 0.1$). Higher conversion was accompanied by hydrogenolysis to *p*-ATL as sole product, possibly *via* consecutive *p*-NBN→*p*-ABN→*p*-ATL. There was no detectable *p*-ABN formation over $Ni/Al_2O_3$ at any conversion with the sole generation of *p*-ATL at *TOF* close to that recorded for $Au/Al_2O_3$ and lower than $Au/ZrO_2$. These results establish superior performance in terms of selectivity for $Au/ZrO_2$ and viable application in the clean continuous production of high value functionalised amines.

## 4. Conclusions

Laboratory synthesised crystalline $ZrO_2$ was used to support Au and employed for the first time in the gas phase continuous hydrogenation of *p*-nitrobenzonitrile (*p*-NBN) to *p*-aminobenzonitrile (*p*-ABN). Precipitation of $ZrOCl_2$ with aqueous $NH_3$ generated amorphous $ZrO_2$ that was transformed to crystalline monoclinic and tetragonal phases following calcination (in air at 673-1073 K). Higher calcination temperatures increased the monoclinic content with a concomitant decrease in surface area/pore volume and increase in crystallite size. Introduction

of Au to (calcined) $ZrO_2$ by deposition-precipitation facilitated tetragonal→monoclinic phase transformation. Temperature programmed reduction of $Au/ZrO_2$ to 473 K served to reduce the Au precursor where higher temperatures resulted in a partial reduction of the support. TEM analysis established quasi-spherical supported Au particles at the nano-scale (3-13 nm) with electron transfer (based on XPS) to generate $Au^{\delta-}$. Conversion of *p*-NBN over $Au/ZrO_2$ and $Au/Al_2O_3$ was fully selective to the target *p*-ABN. $Au/ZrO_2$ delivered higher *TOF* that is linked to a greater $H_2$ chemisorption capacity under reaction conditions and more effective $–NO_2$ activation. $Au/ZrO_2$ outperformed $Pd/Al_2O_3$ and $Ni/Al_2O_3$ where Pd was only selective to *p*-ABN at low conversions with preferential formation of *p*-aminotoluene (*p*-ATL) at high conversion; Ni was non-selective and generated *p*-ATL at all levels of conversion.

**Acknowledgements**

We acknowledge the contribution of Dr. N. Perret to this work. EPSRC support for free access to the TEM/SEM facility at the University of St Andrews and financial support to Dr. X. Wang and Y. Hao through the Overseas Research Students Award Scheme (ORSAS) are also acknowledged.

## References

[1] M. Fornabaio, P. Palmero, R. Traverso, C. Esnouf, H. Reveron, J. Chevalier, L. Montanaro, J. Eur. Ceram. Soc. 35 (2015) 4039-4049.

[2] A.V. Chadwick, G. Mountjoy, V.M. Nield, I.J.F. Poplett, M.E. Smith, J.H. Strange, M.G. Tucker, Chem. Mater. 13 (2001) 1219-1229.

[3] T. Yamaguchi, Catal. Today 20 (1994) 199-217.

[4] J. D' Souza, N. Nagaraju, Indian J. Chem. Technol. 11 (2004) 401-409.

[5] K.J. Ratnam, R.S. Reddy, N.S. Sekhar, M.L. Kantam, F. Figueras, J. Mol. Catal. A: Chem. 276 (2007) 230-234.

[6] S.-T. Wong, C.-C. Hwang, C.-Y. Mou, Appl. Catal. B: Environ. 63 (2006) 1-8.

[7] A.H. Hoveyda, J.P. Morken, A.F. Houri, Z. Xu, J. Am. Chem. Soc. 114 (1992) 6692-6697.

[8] T. Gehrmann, J. Lloret Fillol, S.A. Scholl, H. Wadepohl, L.H. Gade, Angew. Chem. Int. Ed. 50 (2011) 5757-5761.

[9] X.M. Song, A. Sayari, Catal. Rev. 38 (1996) 329-412.

[10] F.R. van den Berg, M.W.J. Craje, A.M. van der Kraan, J.W. Geus, Appl. Catal. A: Gen. 242 (2003) 403-416.

[11] Y. Liu, K. Fang, J. Chen, Y. Sun, Green Chem. 9 (2007) 611-615.

[12] J.-L. Bi, Y.-Y. Hong, C.-C. Lee, C.-T. Yeh, C.-B. Wang, Catal. Today 129 (2007) 322-329.

[13] S. Li, C. Zhang, P. Zhang, G. Wu, X. Ma, J. Gong, Phys. Chem. Chem. Phys. 14 (2012) 4066-4069.

[14] A. Sharma, J. Environ. Eng. 132 (2006) 956-959.

[15] A.S.K. Hashmi, G.J. Hutchings, Angew. Chem. Int. Ed. 45 (2006) 7896-7936.

[16] A. Corma, H. Garcia, Chem. Soc. Rev. 37 (2008) 2096-2126.

[17] J. Gong, Chem. Rev. 112 (2012) 2987-3054.

[18] X. Wang, M. Li, M.A. Keane, in: Z. Ma, S. Dai (Eds.), Heterogeneous Gold Catalysts and Catalysis, The Royal Society of Chemistry, Cambridge, 2014, pp. 424-461.

[19] V. Idakiev, T. Tabakova, A. Naydenov, Z.Y. Yuan, B.L. Su, Appl. Catal. B: Environ. 63 (2006) 178-186.

[20] X. Zhang, H. Wang, B.-Q. Xu, J. Phys. Chem. B 109 (2005) 9678-9683.

[21] C. Wu, Z. Zhang, Q. Zhu, H. Han, Y. Yang, B. Han, Green Chem. 17 (2015) 1467-1472.

[22] Y. Zhang, X. Cui, F. Shi, Y. Deng, Chem. Rev. 112 (2012) 2467-2505.

[23] R.A. Koeppel, A. Baiker, C. Schild, A. Wokaun, J. Chem. Soc.-Faraday Trans. 87 (1991) 2821-2828.

[24] S. Li, C. Zhang, Z. Huang, G. Wu, J. Gong, Chem. Commun. 49 (2013) 4226-4228.

[25] D.P. He, H. Shi, Y. Wu, B.Q. Xu, Green Chem. 9 (2007) 849-851.

[26] A. Corma, C. González-Arellano, M. Iglesias, F. Sánchez, Appl. Catal. A: Gen. 356 (2009) 99-102.

[27] A. Corma, P. Serna, Science 313 (2006) 332-334.

[28] R.J. Rahaim, R.E. Maleczka, Org. Lett. 7 (2005) 5087-5090.

[29] U. Sharma, P.K. Verma, N. Kumar, V. Kumar, M. Bala, B. Singh, Chem.-Eur. J. 17 (2011) 5903-5907.

[30] U. Sharma, P. Kumar, N. Kumar, V. Kumar, B. Singh, Adv. Synth. Catal. 352 (2010) 1834-1840.

[31] K. Koprivova, L. Cerveny, Res. Chem. Intermediat. 34 (2008) 93-101.

[32] K. Hata, K.-I. Watanabe, Bull. Chem. Soc. Jpn. 32 (1959) 861-867.

[33] L. Pehlivan, E. Metay, S. Laval, W. Dayoub, P. Demonchaux, G. Mignani, M. Lemaire, Tetrahedron Lett. 51 (2010) 1939-1941.

[34] X. Wang, N. Perret, M.A. Keane, Chem. Eng. J. 210 (2012) 103-113.

[35] X. Wang, N. Perret, M.A. Keane, Appl. Catal. A: Gen. 467 (2013) 575-584.

[36] N. Perret, F. Cárdenas-Lizana, M.A. Keane, Catal. Commun. 16 (2011) 159-164.

[37] J. Jia, K. Haraki, J.N. Kondo, K. Domen, K. Tamaru, J. Phys. Chem. B 104 (2000) 11153-11156.

[38] H. Moll, H. Musso, H. Schröder, Angew. Chem. Int. Ed. 2 (1963) 212-212.

[39] F. Cárdenas-Lizana, S. Gómez-Quero, M.A. Keane, Appl. Catal. A: Gen. 334 (2008) 199-206.

[40] N. Perret, X. Wang, L. Delannoy, C. Potvin, C. Louis, M.A. Keane, J. Catal. 286 (2012) 172-183.

[41] H. Toraya, M. Yoshimura, S. Somiya, J. Am. Ceram. Soc. 67 (1984) C-119-C-121.

[42] F. Cárdenas-Lizana, X. Wang, D. Lamey, M. Li, M.A. Keane, L. Kiwi-Minsker, Chem. Eng. J. 255 (2014) 695-704.

[43] G.K. Chuah, S. Jaenicke, S.A. Cheong, K.S. Chan, Appl. Catal. A: Gen. 145 (1996) 267-284.

[44] S.-F. Yin, B.-Q. Xu, Chem. Phys. Chem. 4 (2003) 277-281.

[45] P.D.L. Mercera, J.G. Van Ommen, E.B.M. Doesburg, A.J. Burggraaf, J.R.H. Ross, Appl. Catal. 57 (1990) 127-148.

[46] X. Zhang, H. Shi, B.-Q. Xu, Catal. Today 122 (2007) 330-337.

[47] S. Xie, E. Iglesia, A.T. Bell, Chem. Mater. 12 (2000) 2442-2447.

[48] C. Su, D. He, J. Li, Z. Chen, Q. Zhu, J. Mol. Catal. A: Chem. 153 (2000) 139-146.

[49] Z. Xu, L. Chen, Y. Shao, D. Yin, S. Zheng, Ind. Eng. Chem. Res. 48 (2009) 8356-8363.

[50] W. Stichert, F. Schuth, Chem. Mater. 10 (1998) 2020-2026.

[51] G.C. Bond, C. Louis, D.T. Thompson, Catalysis by Gold, Imperial College Press, London, 2006.

[52] S. Ardizzone, C.L. Bianchi, J. Electroanal. Chem. 465 (1999) 136-141.

[53] S. Ardizzone, M.G. Cattania, P. Lugo, Electrochim. Acta 39 (1994) 1509-1517.

[54] F. Moreau, G.C. Bond, Appl. Catal. A: Gen. 302 (2006) 110-117.

[55] R. Zanella, C. Louis, Catal. Today 107-108 (2005) 768-777.

[56] F. Moreau, G.C. Bond, A.O. Taylor, J. Catal. 231 (2005) 105-114.

[57] F.B. Noronha, E.C. Fendley, R.R. Soares, W.E. Alvarez, D.E. Resasco, Chem. Eng. J. 82 (2001) 21-31.

[58] X. Zhang, H. Shi, B.-Q. Xu, Angew. Chem. Int. Ed. 44 (2005) 7132-7135.

[59] X. Wang, N. Perret, J.J. Delgado, G. Blanco, X. Chen, C.M. Olmos, S. Bernal, M.A. Keane, J. Phys. Chem. C 117 (2013) 994-1005.

[60] F. Cárdenas-Lizana, S. Gómez-Quero, N. Perret, M.A. Keane, Catal. Sci. Tech. 1 (2011) 652-661.

[61] R. Grau-Crespo, N.C. Hernandez, J.F. Sanz, N.H. de Leeuw, J. Mater. Chem. 19 (2009) 710-717.

[62] J.A. Lopez-Sanchez, D. Lennon, Appl. Catal. A: Gen. 291 (2005) 230-237.

[63] S.Y. Liu, S.M. Yang, Appl. Catal. A: Gen. 334 (2008) 92-99.

[64] G.C. Bond, Molecules 17 (2012) 1716-1743.

[65] C. Kartusch, J.A. van Bokhoven, Gold Bull. 42 (2009) 343-348.

[66] E. Bus, J.T. Miller, J.A. van Bokhoven, J. Phys. Chem. B 109 (2005) 14581-14587.

[67] M. Boronat, F. Illas, A. Corma, J. Phys. Chem. A 113 (2009) 3750-3757.

[68] A. Alshammari, A. Köckritz, V.N. Kalevaru, A. Bagabas, A. Martin, Appl. Petrochem. Res. 2 (2012) 61-67.

[69] S. Arrii, F. Morfin, A.J. Renouprez, J.L. Rousset, J. Am. Chem. Soc. 126 (2004) 1199-1205.

[70] N. Kruse, S. Chenakin, Appl. Catal. A: Gen. 391 (2011) 367-376.

[71] B. Ealet, E. Gillet, Surf. Sci. 367 (1996) 221-230.

[72] K.-I. Shimizu, Y. Miyamoto, T. Kawasaki, T. Tanji, Y. Tai, A. Satsuma, J. Phys. Chem. C 113 (2009) 17803-17810.

[73] W.C. Conner, J.L. Falconer, Chem. Rev. 95 (1995) 759-788.

[74] X. Wang, F. Cárdenas-Lizana, M.A. Keane, ACS Sustainable Chem. Eng. 2 (2014) 2781-2789.

## Figure Captions

**Fig. 1**: (A) Temporal pH variation in the preparation of $ZrO_2$; (B) XRD patterns of $ZrO_2$ calcined at (I) 673 K, (II) 723 K and (III) 973 K; (C) Temporal pH and temperature variation in the preparation of $Au/ZrO_2$. *Note*: dashed line identifies $pH_{PZC}$ of the $ZrO_2$ support; (D) XRD pattern for $Au/ZrO_2$.

**Fig. 2**: Nitrogen adsorption (open symbols) and desorption (solid symbols) isotherms with associated pore size distributions for (A) $ZrO_2$ (post calcination at 673 K) and (B) $Au/ZrO_2$ (post TPR at 473 K).

**Fig. 3**: (A) Temperature programmed reduction (TPR) profiles (10 K $min^{-1}$ to 1073 K) for (I) $ZrO_2$ and (II) $Au/ZrO_2$; (B) TPR profiles (2 K $min^{-1}$ to 473 K) for (I) $Au/ZrO_2$ and (II) $Au/Al_2O_3$.

**Fig. 4**: Gold particle size distribution histograms with representative TEM images (inset) for (A) $Au/ZrO_2$ and (B) $Au/Al_2O_3$.

**Fig. 5**: XPS spectra over the Au 4*f* region for (I) $Au/ZrO_2$ and (II) $Au/Al_2O_3$.

**Fig. 6**: Reaction pathways associated with the hydrogenation of *p*-NBN, identifying steps observed in this study (solid arrows) and additional steps reported in the literature [28,31-33] (dashed arrows).

**Fig. 7**: (A) Time on-stream variation of *p*-NBN fractional conversion ($x_{p\text{-}NBN}$) over $Au/ZrO_2$ (■) and $Au/Al_2O_3$ (○): $n/F$: 1.6-5.4 × $10^{-2}$ h; lines represent fit to eq. (4). (B) *p*-ABN selectivity ($S_{p\text{-}ABN}$) as a function of $x_{p\text{-}NBN}$ over $Au/ZrO_2$ (▲) and $Au/Al_2O_3$ (×); inset: pseudo-first order kinetic plots for reaction over $Au/ZrO_2$ (■) and $Au/Al_2O_3$ (○).

**Fig. 1**

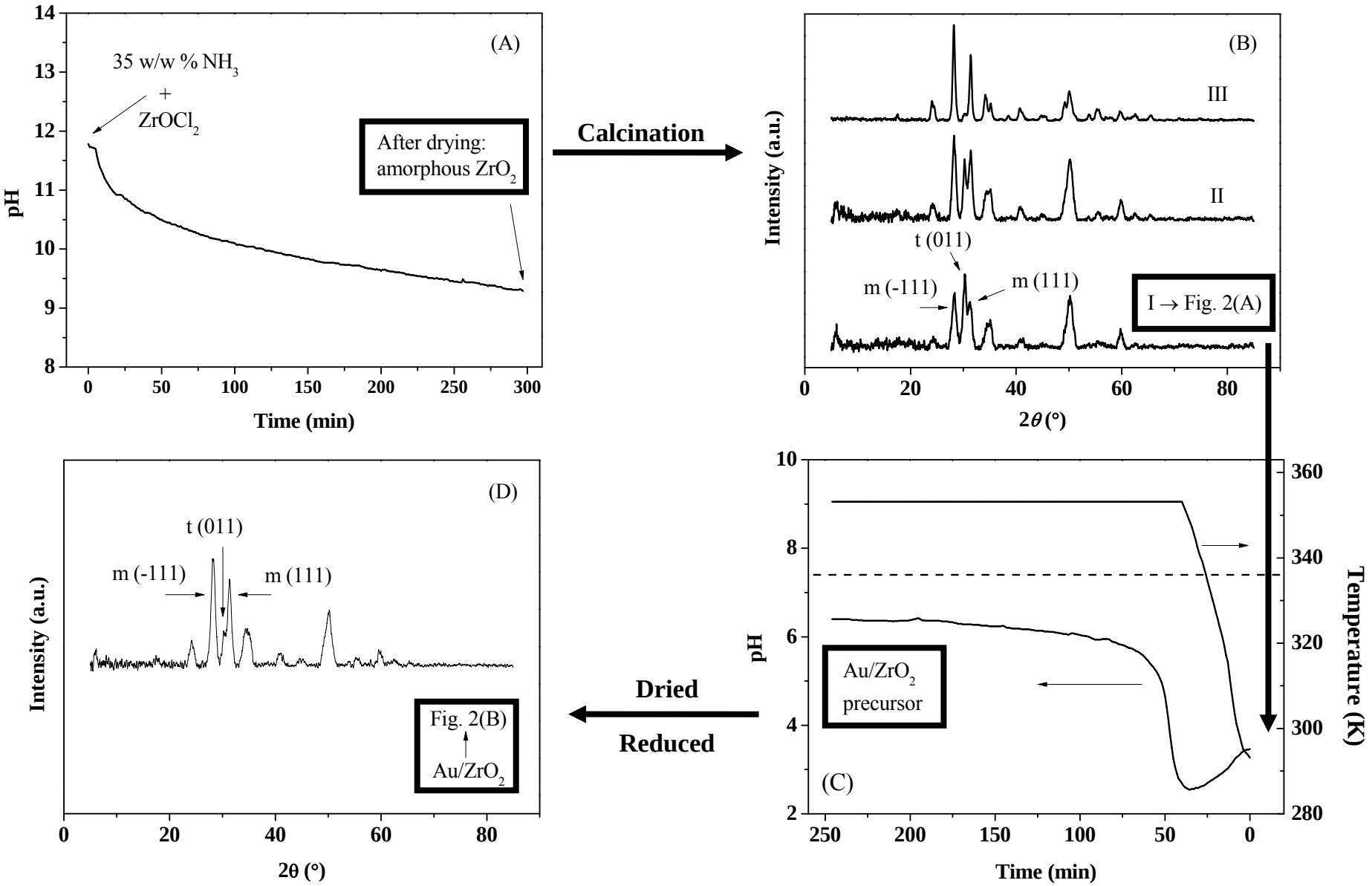
(A)
35 w/w % NH3
+
ZrOCl2
After drying:
amorphous ZrO2
pH
Time (min)
Calcination
(B)
III
II
t (011)
m (-111)
m (111)
I → Fig. 2(A)
Intensity (a.u.)
2θ (°)
(C)
Au/ZrO2
precursor
pH
Temperature (K)
Time (min)
Dried
Reduced
(D)
t (011)
m (-111)
m (111)
Fig. 2(B)
Au/ZrO2
Intensity (a.u.)
2θ (°)

**Fig. 2**

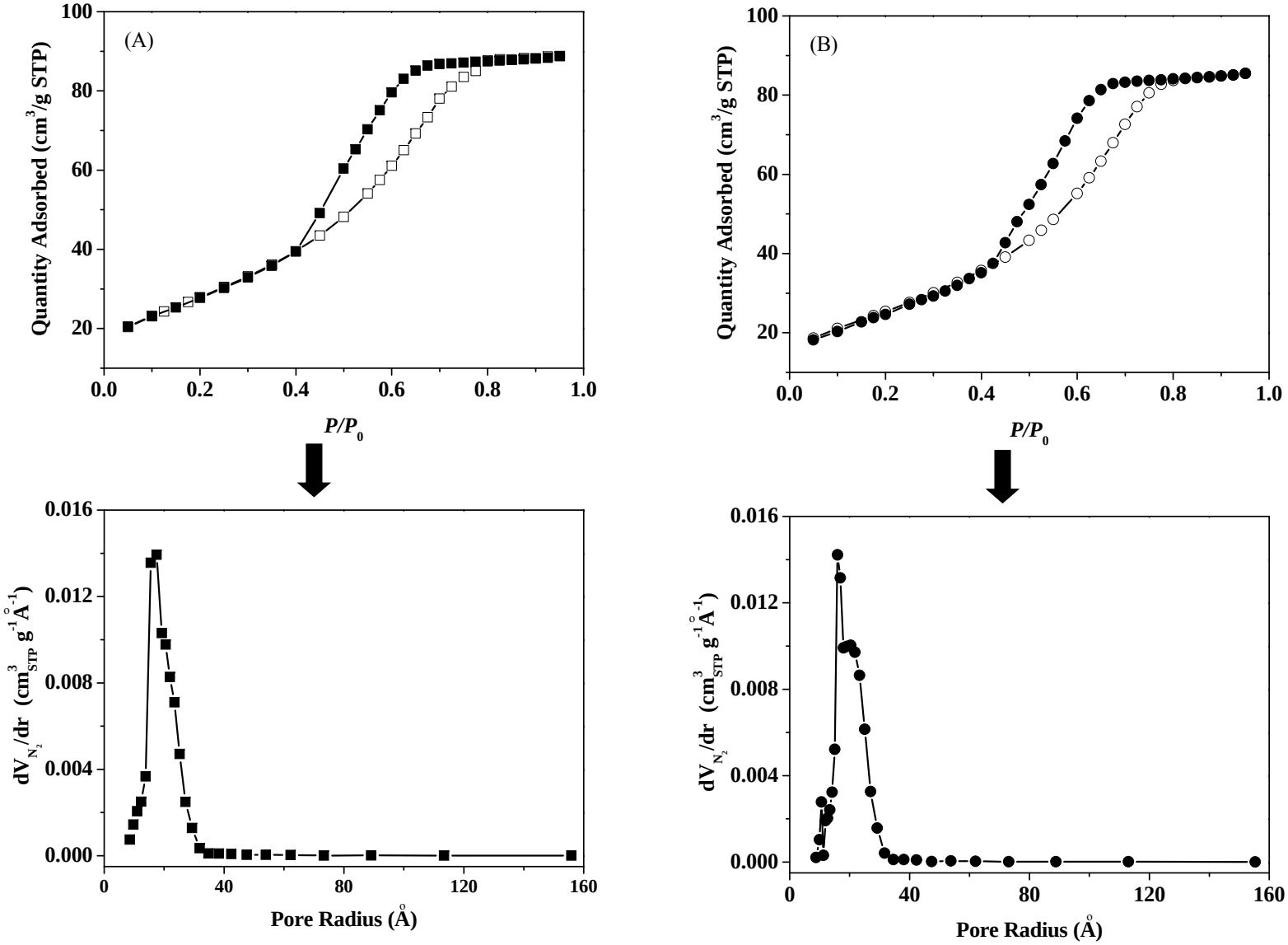
(A)
(B)
Quantity Adsorbed (cm³/g STP)
P/P0
dV N2 /dr (cm³STP g⁻¹ Å⁻¹)
Pore Radius (Å)

**Fig. 3**

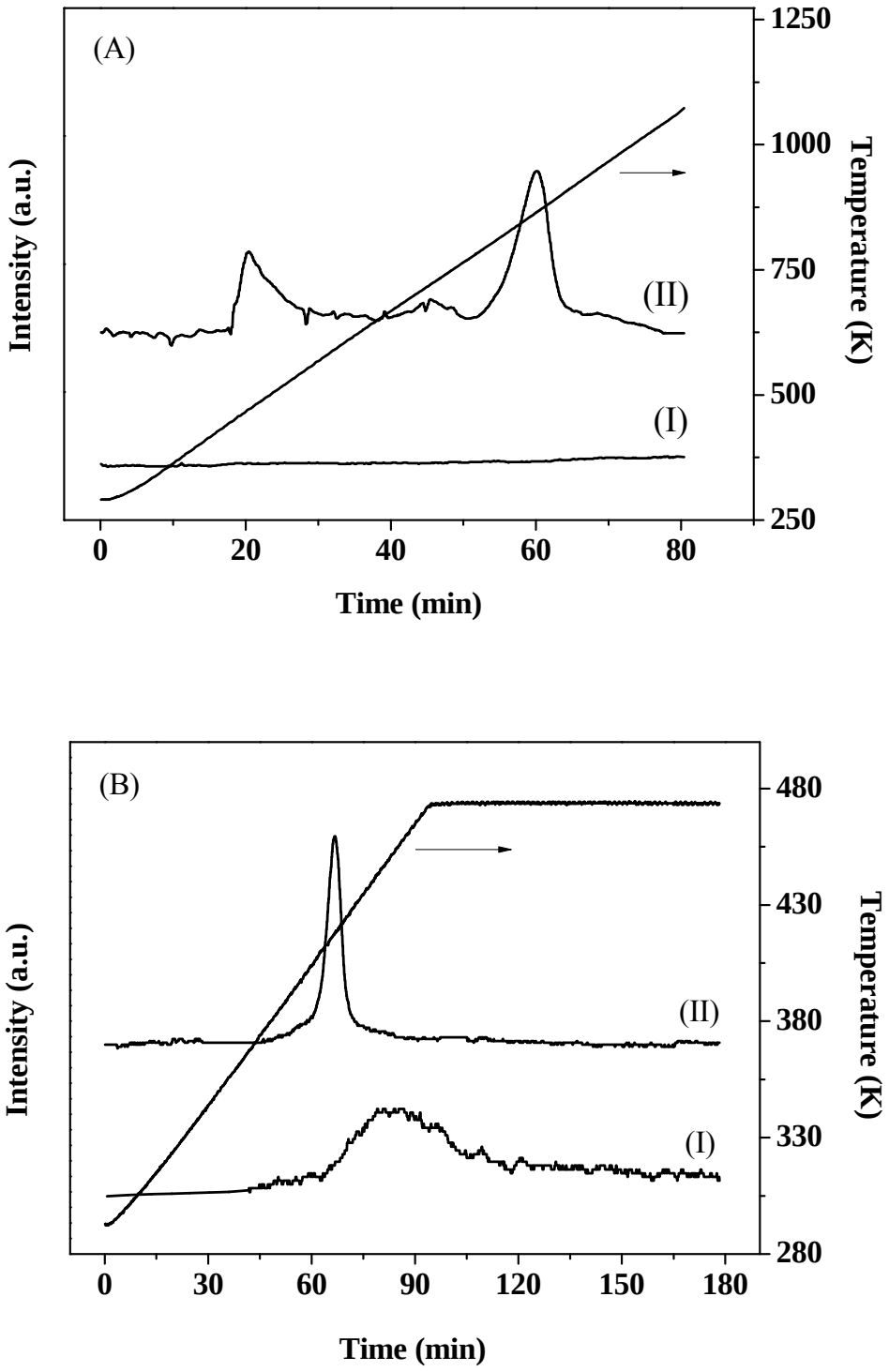

**Fig. 4**

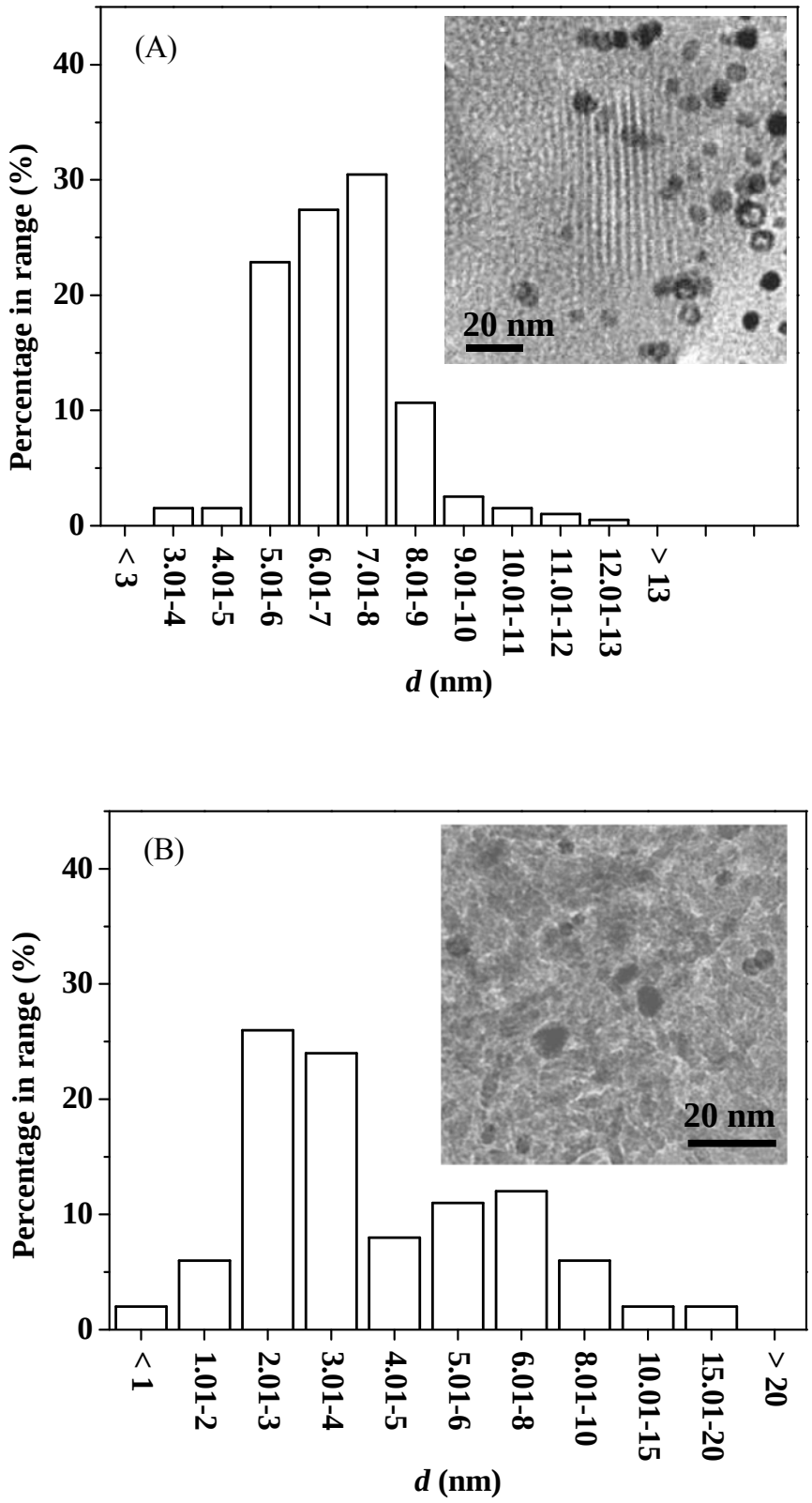

**Fig. 5**

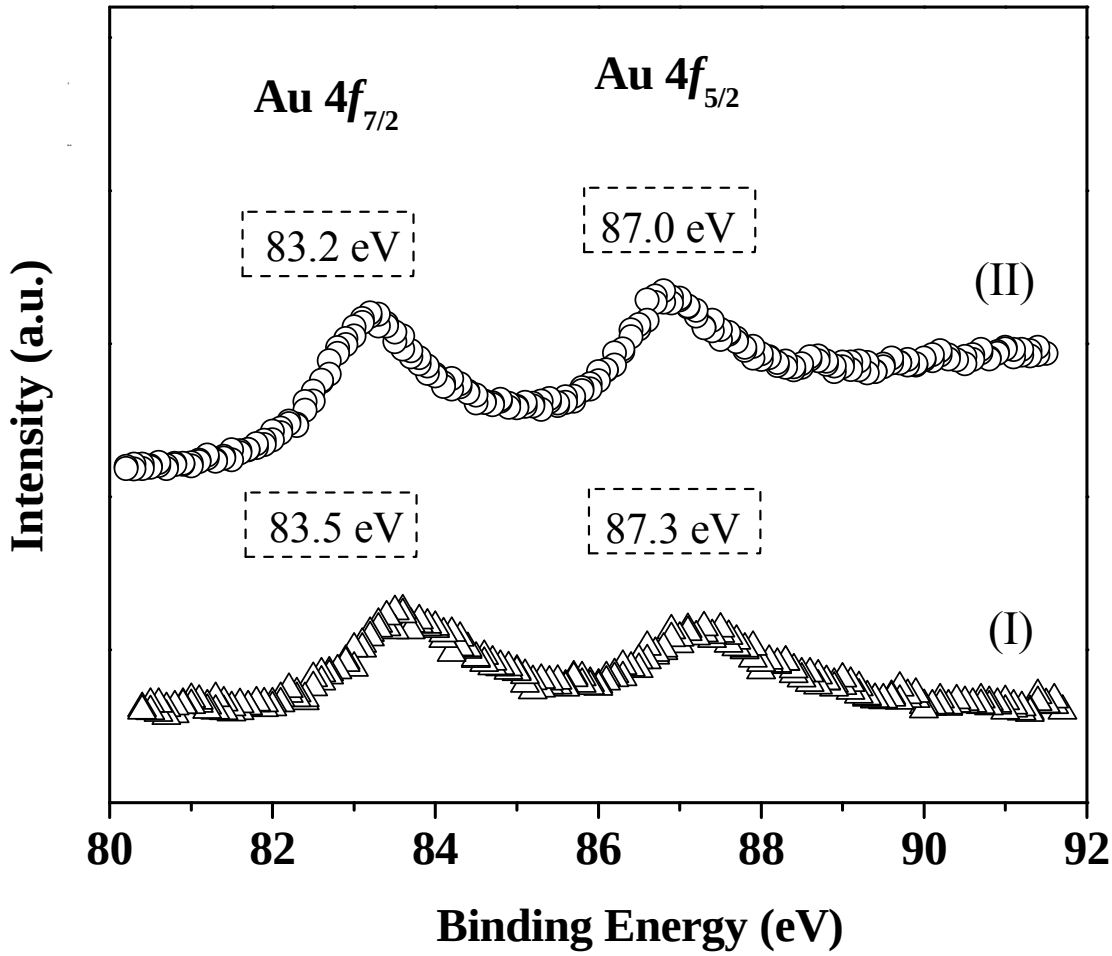

**Fig. 6**

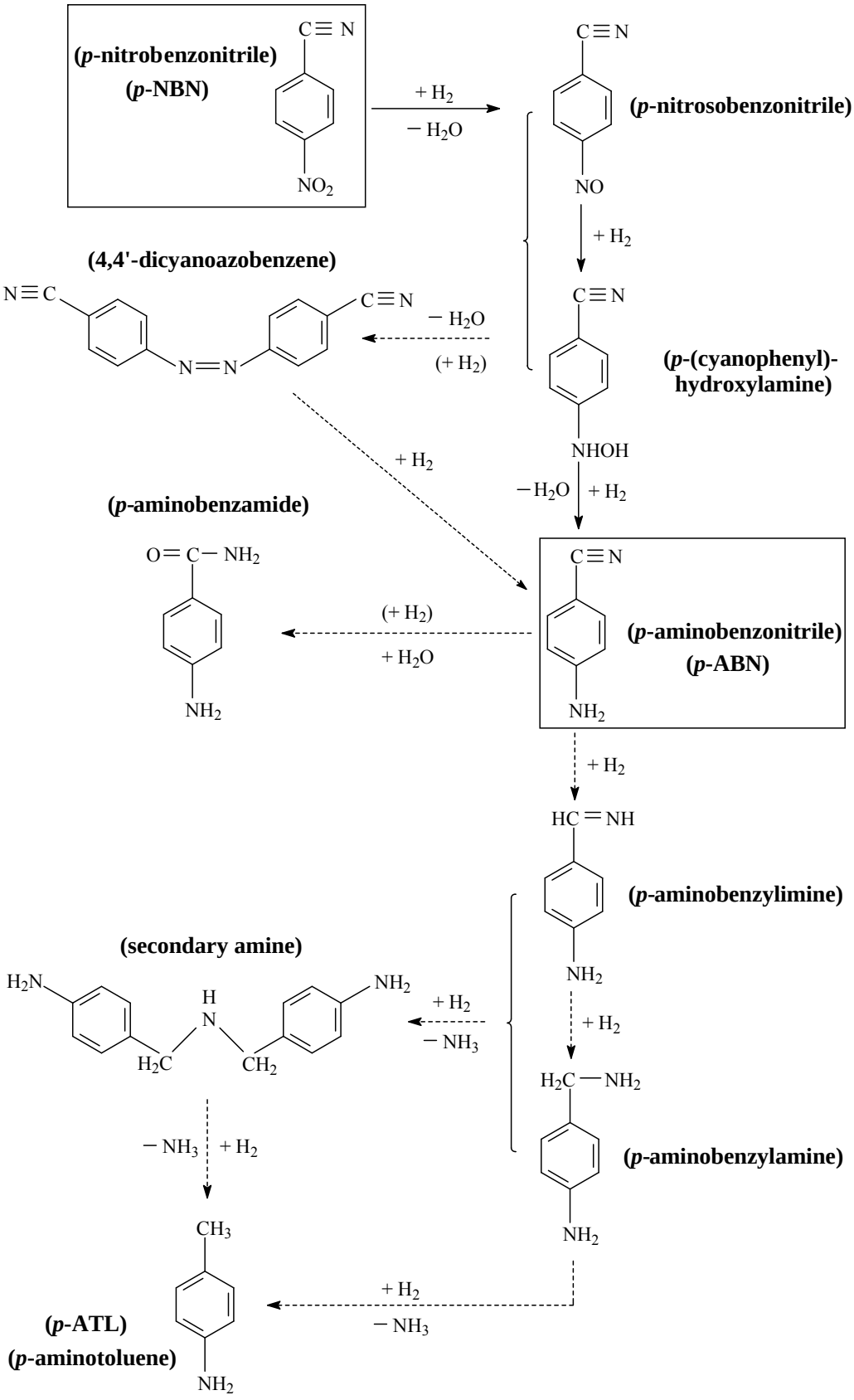

**Fig. 7**

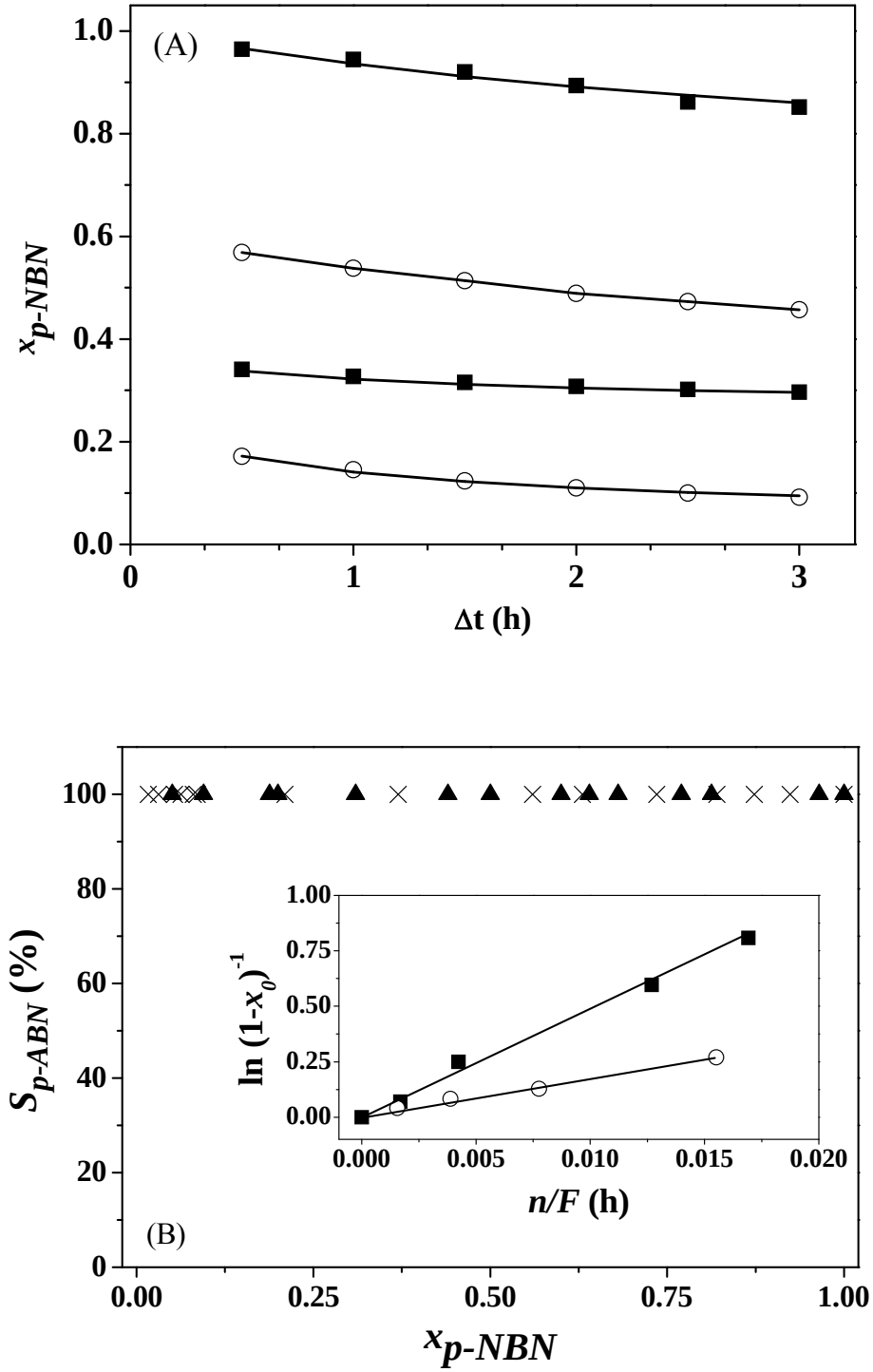

**Table 1**: BET surface area, porosity and crystallinity characteristics of $ZrO_2$ and $Au/ZrO_2$.

| Sample (calcination temperature) | BET surface area ($m^2\ g^{-1}$)[a] | Total pore volume ($cm^3\ g^{-1}$)[b] | Mean pore radius (Å)[b] | Monoclinic phase (%) | Crystallite size (nm)[c] |
|---|---|---|---|---|---|
| $ZrO_2$[d] | 280 (289 [44,45]) | 0.19 (0.19 [45]) | 14 | - | - |
| $ZrO_2$ (673 K) | 104 (120 [46],123 [25],110 [3]) | 0.14 (0.16 [46]) | 19 | 58 | 10.7 |
| $ZrO_2$ (723 K) | 89 | 0.09 | 15 | 72 | 11.8 |
| $ZrO_2$ (973 K) | 25 (22 [3],40 [47],13 [48]) | 0.07 | 31 | 97 (96 [49]) | 16.2 |
| $Au/ZrO_2$[e] | 93 | 0.13 | 19 | 88 | 11.6 |

[a]values quoted in the literature are given in parentheses

[b]from BJH analysis

[c]calculated using Scherrer formula from (-111) and (111) peaks for monoclinic $ZrO_2$ and (011) peak for tetragonal $ZrO_2$

[d]sample as prepared (and dried at 373 K)

[e]$ZrO_2$ calcined at 673 K

**Table 2:** Physicochemical characteristics of $Au/ZrO_2$ and $Au/Al_2O_3$.

| Catalyst | $Au/ZrO_2$ | $Au/Al_2O_3$ |
|---|---|---|
| Au loading (% w/w) | 0.8 | 1.1 |
| BET surface area ($m^2\ g^{-1}$) | 93 | 161 |
| Total pore volume ($cm^3\ g^{-1}$) | 0.13 | 0.36 |
| Mean pore radius (Å) | 19 | 30 |
| TPR $T_{max}$ (K) | 452 | 417 |
| TPR $H_2$ consumed (mmol $g_{Au}^{-1}$) | 7.0 | 7.1 |
| $H_2$ chemisorption (µmol $g_{Au}^{-1}$)[a] | 56 | 19 |
| $H_2$ chemisorption (µmol $g_{Au}^{-1}$)[b] | 154 | 61 |
| $H_2$ desorbed (mmol $g_{Au}^{-1}$) | 28 | 24 |
| $d_{TEM}$ (nm) | 7.0 | 7.8 |
| Dispersion (*D*) *(%)* | 18 | 16 |
| XPS binding energy (Au $4f_{7/2}$) | 83.5 | 83.2 |

[a]at ambient temperature
[b]at reaction temperature (423 K)

**Table 3.** Catalytic performance of $Au/ZrO_2$, $Au/Al_2O_3$, $Pd/Al_2O_3$ and $Ni/Al_2O_3$ in terms of *p*-NBN turnover frequency (*TOF*) and *p*-ABN selectivity ($S_{p\text{-}ABN}$) at partial ($x = 0.1$) and complete ($x = 1$) *p*-NBN conversion.

| Catalyst | *TOF* ($h^{-1}$) | $S_{p\text{-}ABN}$ (%) at $x_{p\text{-}NBN} = 0.1$ | $S_{p\text{-}ABN}$ (%) at $x_{p\text{-}NBN} = 1$ |
|---|---|---|---|
| $Au/ZrO_2$ | 267 | 100 | 100 |
| $Au/Al_2O_3$ | 109 | 100 | 100 |
| $Pd/Al_2O_3$[a] | 1717 | 100 | 0[b] |
| $Ni/Al_2O_3$[a] | 123 | 0[b] | 0[b] |

[a] $x_{p\text{-}NBN} = 0.1$ obtained using 10% v/v $H_2$ in He as carrier gas

[b] *p*-aminotoluene (*p*-ATL) was the sole product